





Velocity-mapped imaging of electron dynamics in an ultracold laser-induced plasma

Eric James Smoll, Jr. , Irina Jana, Jonathan H. Frank , and David W. Chandler ^{*}
Combustion Research Facility, Sandia National Laboratories, Livermore, California 94550, USA

 (Received 31 March 2023; revised 23 June 2023; accepted 15 August 2023; published 2 October 2023)

We report a time-resolved study on the electron kinetics and dynamics that occur during the formation of an ultracold plasma generated by resonance enhanced multiphoton ionization of krypton in a pulsed supersonic beam. Measurements are performed using a new apparatus that incorporates time-resolved velocity-mapped imaging of the entire electron energy distribution with nanosecond time resolution. We resolve the rapid deceleration and escape of 3.32 eV photoelectrons and the subsequent equilibration, cooling, and escape of electrons that are trapped by the expanding photocation distribution.

DOI: [10.1103/PhysRevA.108.L041301](https://doi.org/10.1103/PhysRevA.108.L041301)

I. INTRODUCTION

Plasmas are a fundamental state of matter and can be prepared from a wide variety of precursor systems in a wide variety of experimental configurations. For example, the ionization needed to prepare a plasma can be supplied by energetic collisions with neutral or charged particles, and strong electric and magnetic fields, or by absorbing electromagnetic radiation [1]. Once formed, the unique physical and chemical behavior of a plasma is ultimately controlled by the evolving speciation and energy distribution of its constituent charged and neutral particles. For this reason, most plasma science and engineering efforts are centered around monitoring, controlling, and correlating plasma speciation and particle energy distributions with desirable plasma behavior such as manipulating electromagnetic radiation [2] or catalyzing important chemical reactions [3–5]. The electron energy distribution function (EEDF) is a particularly important plasma parameter, and there is a need for new EEDF measurement techniques that complement existing capabilities.

Commonly used techniques for EEDF measurements in plasmas include electric probes, optical emission spectroscopy, and Thomson scattering. Langmuir probes are widely used electric probes that are inserted into plasmas and are small compared to the mean free path of plasma electrons. The current-voltage characteristics of Langmuir probes can be used to derive plasma electron density and temperature with high sensitivity [6]. Optical techniques provide noncontact measurements of EEDFs. For Maxwellian electron energy distributions with temperatures between 5 and 200 eV, the intensity ratio of certain plasma ion transitions with a common initial state can be used to extract electron temperature [7]. Stark broadening of two emission lines can be analyzed with the crossing-point method to simultaneously quantify electron density and temperature in atmospheric pressure plasmas with errors of approximately 5% and 10%, respectively [8]. When combined with a kinetic model that relates plasma

temperature to excited state populations of a plasma component such as helium, the intensity of carefully selected emission lines can be used to report on electron density and temperature. Unfortunately, accurate rate constants must be known which limits the utility of line emission measurements to low densities where excitation from the ground state dominates [9]. The spectral line shape of light scattering from high-temperature plasma electrons (Thomson scattering) can be used to derive electron densities and energy distributions without disturbing the plasma or requiring any assumptions of thermodynamic equilibrium. Unfortunately, cross sections for Thomson scattering are five orders of magnitude smaller than other typical cross sections for atomic and molecular interactions, resulting in high requirements for laser power and stray light rejection [10]. Furthermore, Thomson scattering in plasmas containing molecules is subject to significant interference from molecular Raman scattering.

These conventional EEDF measurement techniques are not well suited for ultracold plasmas. One approach that has been used to determine the electron density and temperature in ultracold plasmas bound by space charge is to measure the electron spillover induced by lowering the barrier of the Coulomb potential with a weak applied field [11]. The development of charged particle *imaging* methods that extract quantitative information on electron energy and density is promising. Kroker *et al.* used charged particle trajectory simulations to support the analysis of spatially mapped electron images produced by extracting electrons from an ultracold plasma formed by femtosecond photoionization of rubidium atoms in a high-density Bose-Einstein condensate [12]. Zhang *et al.* used a 4 μ s, high-voltage extraction pulse to collect time-resolved spatially mapped images of electrons and cations in an ultracold plasma formed by photoionization of xenon in a magneto-optical trap [13]. Plasma expansion was observed to be ballistic with a velocity proportional to the initial plasma temperature above ~ 100 K. Below ~ 50 K, plasma expansion was independent of the initial electron energy and proceeded at ~ 50 m/s. Grant and co-workers have explored the microsecond to millisecond timescale dynamics of an ultracold plasma prepared by two-color excitation of

^{*}Corresponding author: chand@sandia.gov

Rydberg states in a pulsed supersonic beam of 10% NO in He [14]. In their experiments, time-resolved data are collected by positioning a detection system at various distances from the laser-interaction region and allowing the velocity of the supersonic beam to carry the plasma through a grounded grid. Beyond the grid, electrons are accelerated and spatially mapped onto a two-dimensional (2D) position sensitive detector. The size, shape, intensity, and time-of-flight spectrum is interpreted with the help of rate equation models.

In the present study, we demonstrate the utility of velocity-mapped imaging (VMI) to measure electron energy distributions. Velocity-mapped imaging has revolutionized experimental physical chemistry by providing a general, high-resolution method to record energy and angular distributions of particle dissociation and scattering in the gas phase [15–21]. Although there are many VMI variants [22], most use electric fields to uniformly accelerate charged particles through an electrostatic lens system onto a position sensitive detector capable of recording individual electron or ion impacts. During this extraction process, the charged particles naturally disperse in space according to their velocity (faster particles expand farther than slower particles). The electrostatic lens is optimized to focus particles with the same three-dimensional (3D) velocity to the same 2D location on a position sensitive detector. This configuration counteracts blurring associated with the initial charged particle volume because the particle trajectories are curved to behave as if they originated from a point source, which greatly improves the velocity resolution. Although VMI has emerged as the most productive tool to study the dynamics of dilute, uncoupled ensembles of neutral and charged gases, little effort has gone into applying VMI to explore the dynamics of coupled ensembles of neutral and charged particles or *plasmas*. In this study, we demonstrate VMI measurements of EEDFs in laser-induced plasmas using an ultrafast extraction pulse in the exploration of the dynamics of plasma induced by 2+1 resonance enhanced multiphoton ionization (REMPI) of Kr in a pulsed supersonic beam.

II. METHODS

Electron energy distributions were measured in laser generated plasmas using a recently developed combined electron-imaging and ion-imaging mass spectrometer. Both the “source” and “main” vacuum chambers are independently pumped by 1800 l/s turbo pumps (Pfeiffer HiPace 1800) backed by dry vacuum pumps (Alcatel Adixen ACP15). In the source vacuum chamber, a cantilever-type piezoelectric valve with a 150 μm nozzle diameter (Amsterdam Pizeovalve ACPV2) is configured to deliver a pulsed supersonic beam of 20% Kr in He or pure Kr from a stagnation pressure of 40 psi at a repetition rate of 10 Hz (see Fig. 1). A 300 μm diameter skimmer (Beam Dynamics) positioned 4 cm from the valve face transmits the central part of the supersonic beam into the main vacuum chamber with a base pressure 1.0×10^{-8} Torr. In the main chamber, the gas pulse enters a stack of 84 mm diameter circular plate electrodes through a 4 mm diameter aperture in the center of the first electrode or “repeller.” The second and third electrodes have a 32 mm diameter aperture covered by a nickel electroformed mesh with a wire density of

117 lines per inch (Precision Electroforming). Electrodes 4–6 define an Einzel lens and have apertures of 60, 32, and 60 mm, respectively. For all the work reported here, electrodes 2, 3, 4, and 6 are grounded.

Midway between the repeller and the first mesh electrode, the pulsed supersonic beam is overlapped with the output of a frequency-doubled Nd:YAG-pumped optical parametric oscillator focused by a 19 cm focal length UV lens. Optical parametric oscillator (OPO) radiation with a bandwidth of 0.2 cm^{-1} and a center wavelength of 214.77 nm was used to induce 2+1 REMPI of Kr. The resulting 3.32 eV photoelectrons were extracted from the interaction region by applying an ultrafast voltage pulse (Kentech PBG1) to the repeller (see Fig. 1). Extracted electrons are directed through the first and second meshes and Einzel lens electrodes before traversing a field-free time-of-flight (TOF) tube to impact the front face of a 75 mm diameter microchannel plate (MCP) detector. The flight path of extracted photoelectrons is shielded from external magnetic fields by a mu-metal cylinder that is perforated to increase pumping conductance. Amplified electrons exit the back of the MCP and are accelerated into a P47 phosphor anode. The resulting emission from the phosphor screen is imaged with a scientific complementary metal-oxide-semiconductor (sCMOS) camera (Andor Marana) controlled by a custom LABVIEW program.

Intensity distributions recorded by the camera are a result of “crushing” 3D velocity distributions (also called Newton spheres) onto a 2D position sensitive detector. The 3D velocity distribution of extracted electrons from low-power photoionization is, in general, cylindrically symmetric about the laser polarization vector. When the laser polarization vector is parallel to the 2D plane of the position sensitive detector, the crushed photoelectron camera image can be numerically postprocessed with an inverse Abel algorithm (PYABEL) to obtain the central slice of the uncrushed velocity distribution, which provides particle speeds as a function of the angle from the axis of symmetry (see Fig. 2). As demonstrated below, electrons that are extracted from laser-induced plasma rapidly develop spherical symmetry in the 3D velocity distribution (nonsymmetric distributions at short times can only be quantitatively interpreted by simulating the ultracold plasma dynamics and charged particle extraction trajectories). When the 3D velocity distribution is spherically symmetric, the crushed electron image can be vertically binned to obtain the uncrushed velocity distribution in the horizontal direction. We find that horizontal velocity distributions are reasonably well described by a single Gaussian distribution at extraction times longer than $\sim 0.5\ \mu\text{s}$. Gaussian fits were used to assign a temperature to specific horizontal velocity distributions (discussed below). To interrogate plasma formation and evolution under field-free conditions, a subnanosecond $-4500\ \text{V}$ pulse is used to extract electrons and VMI conditions are obtained by applying $-370\ \text{V}$ to the center Einzel lens electrode (see Figs. 1 and 2).

III. RESULTS AND DISCUSSION

We selected 2+1 REMPI of Kr to demonstrate ultrafast pulsed electron extraction and velocity-mapped imaging of laser-induced plasma because it represents a local optimum

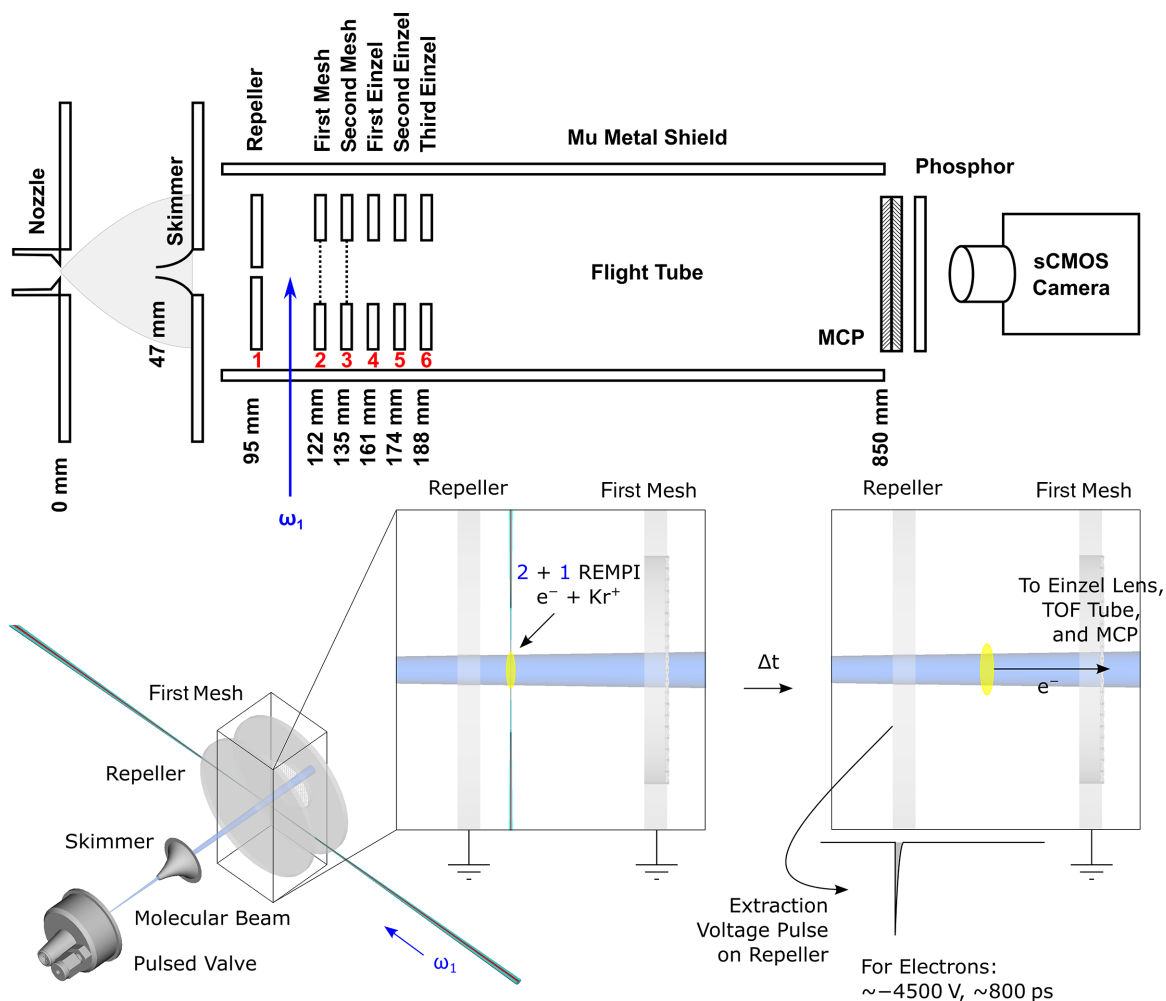


FIG. 1. Schematics of the velocity-mapped imaging plasma spectrometer. Electrodes are given descriptive names in black and referenced according to number in red. Bottom row shows two-step sequence of laser photoionization in a field-free environment followed by pulsed extraction of electrons.

in laser power requirements, charge density achieved with focused laser light, and total charge created for maximum signal and sensitivity. Although the bandwidth of the

214.77 nm laser light generated by the optical parametric oscillator is one to two orders of magnitude larger than the bandwidth expected from single and dual grating nanosecond

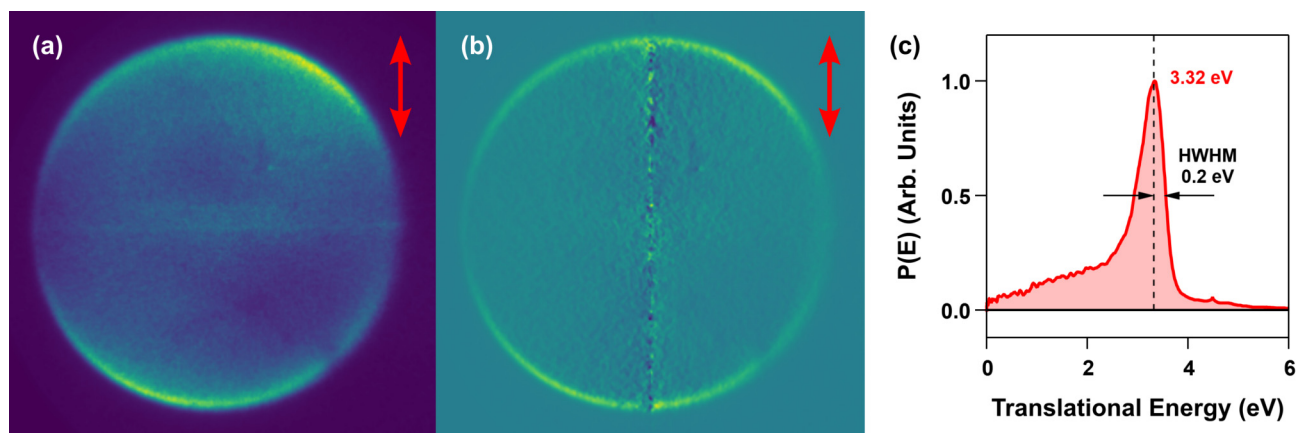


FIG. 2. (a) Raw velocity-mapped image of 3.32 eV electrons from 2+1 REMPI of krypton at 214.77 nm extracted with an ultrafast, high-voltage repeller pulse under low laser power conditions where ultracold plasma is not formed. (b) Inverse Abel transformation of the raw velocity-mapped image shown on the left. Red arrows indicate the orientation of the laser polarization vector. (c) Apparent electron energy distribution obtained by integrating over the electron emission angle in (b).

pulsed dye lasers, the pulse energy provides efficient two-photon excitation of the $5p[3/2]_2$ intermediate state of Kr by pairing photons above and below the center wavelength. The true energy bandwidth of the photoelectrons generated by one-photon ionization of the $5p[3/2]_2$ intermediate state is dictated by the optical parametric oscillator bandwidth, which should be less than 0.2 cm^{-1} ($2.5 \times 10^{-5}\text{ eV}$). The apparent bandwidth of the electron energy distribution shown in Fig. 2 is much larger than the true bandwidth of the OPO excited 2+1 REMPI of Kr because of the instrument response function of the ultrafast pulsed extraction VMI spectrometer at 3.32 eV. This energy resolution is dependent on many factors including the shape of the voltage pulse on the repeller, the design of the ion optics, and various forms of dispersion in charged particle trajectories caused by nonideal starting positions and velocities. For the current system, we estimate that the energy resolution for detecting 3.32 eV electrons is 0.4 eV. This estimate is obtained by evaluating the half width at half maximum (HWHM) of the outer edge of the energy distribution in Fig. 2(b) and doubling the value. In the limit that the velocity resolution is constant across the image, the corresponding energy resolution increases with \sqrt{E} as $E \rightarrow 0$, providing improved energy resolution as extracted electron distributions become colder [17]. Velocity resolution in the plasma imaging mass spectrometer should linearly increase with flight time to the position sensitive detector but is fundamentally limited by the repeller voltage necessary to extract all electrons from the plasma Coulomb potential. In a separate set of experiments using photoionization of NO to generate very low electron energies of 0.04 eV, this VMI apparatus was capable of resolving electron energies with tens of meV.

For laser pulse energies below 1 μJ , the REMPI rate is low and measurements of the mostly unperturbed photoelectron energy and angular distributions can be used to characterize and calibrate the imaging mass spectrometer. For these laser pulse energies, no extracted electrons are detected by the imaging system when the ultrafast, high-voltage repeller pulse is delayed by more than $\sim 15\text{ ns}$. This short time span of the electron signal implies that all photoelectrons promptly escape from the initial ionization volume without being trapped by the photocation distribution to produce a plasma: 3.32 eV electrons travel at $\sim 1\text{ mm/ns}$ and should leave the interaction region and collide with the grounded metallic components in the main vacuum chamber within $\sim 15\text{ ns}$. In contrast, for a pulse energy of 80 μJ , the REMPI rate produces a sufficient cation charge density to decelerate a significant fraction of the escaping photoelectrons resulting in the appearance of a long tail at low energies in the velocity-mapped image (not shown). At this high pulse energy, the imaging system is able to detect electron signals when the extraction pulse is delayed by hundreds or thousands of nanoseconds after the REMPI laser pulse. This persistence of electron signal is clear evidence that some fraction of photoelectrons is trapped in the interaction region.

Electron trapping induced by photoionizing large fractions of a noble gas at the densities achieved in a skimmed molecular beam is expected and consistent with early work using two-color photoionization of xenon [23]. In general, distributions of electrons and cations evolve into a plasma

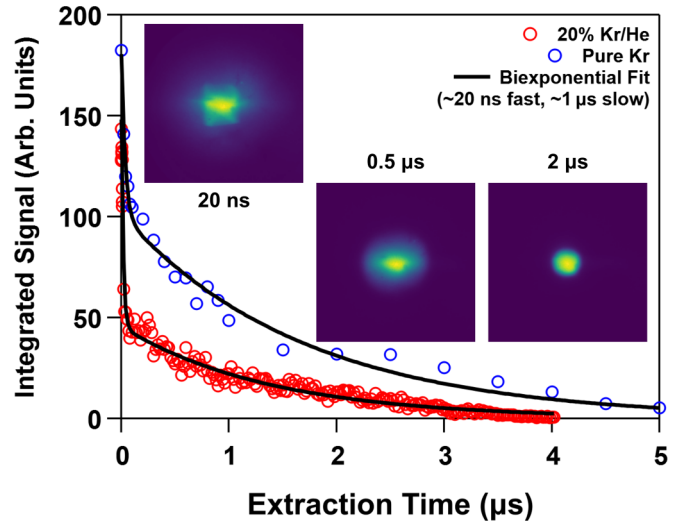


FIG. 3. Variation in the total extracted electron signal obtained by integrating velocity-mapped images as a function of extraction time. Bimodal kinetics are observed for both pure Kr and 20% Kr in He. The short and long timescales are associated with the detection of electrons that are not trapped and trapped, respectively. Representative velocity-mapped images at 20 ns, 0.5 μs , and 2 μs are inset.

when the Debye screening length falls below the characteristic size of the system. For plasmas prepared by photoionization of atoms and molecules in a pulsed supersonic beam, this criterion is mathematically equivalent to the threshold photocation density needed to produce a potential well that matches the photoelectron energy and traps the electrons [23,24]. For photoelectron energies that exceed $\sim 100\text{ cm}^{-1}$, recombination with atomic cations is improbable resulting in a simple, collisionless, self-similar plasma expansion into vacuum for an initially spherical Gaussian charge distribution [25]. This regime of “limited complexity” with an atomic beam is well suited for the development of new experimental methods.

Figure 3 demonstrates the extraction of plasma kinetic information by monitoring the total intensity of VMI images as a function of extraction time with nanosecond resolution. For both pure Kr and 20% Kr in He, the extracted electron signal is observed to decay with both a fast timescale and a slow timescale. We associate the fast timescale ($\tau \sim 20\text{ ns}$) with decelerated REMPI electrons that escape to produce a net-positive charge distribution with a potential well deep enough to trap the remaining 3.32 eV photoelectrons. The resulting electron trapping fractions are 31% for the Kr/He mixture and 56% for pure Kr. These trapping fractions are consistent with expectation: for the same laser power, more photocations are produced in pure Kr relative to the Kr/He mix. More photocations translate to a larger fraction of trapped electrons. The observed trapping fractions are also qualitatively consistent with an estimate of the “trapping threshold” defined as the minimum number of cations necessary to trap a single 3.32 eV photoelectron. Idealized hydrodynamic calculations predict a center-line atomic beam density of $2.3 \times 10^{19}\text{ m}^{-3}$ for pure Kr at the interaction region [26]. Density matrix rate equation calculations suggest that $\sim 10\%$ of the atomic beam is ionized by 80 μJ of 214.7 nm laser light with a

bandwidth of 0.2 cm^{-1} [27]. We estimate a REMPI excitation volume of $2.4 \times 10^{-11} \text{ m}^3$ (aspect ratio ~ 6) by combining a profiling camera measurement of the laser beam waist with an assumed Gaussian transverse profile of the skimmed atomic beam. Thus, from laser and atomic beam parameters, we estimate the production of approximately 60 000 000 photocations per laser shot ($N_i = N_e$). From the dimensions of the REMPI excitation volume, we calculate the cation potential well to be $\sim 1 \times 10^{-5} \text{ eV/cation}$ which corresponds to a trapping threshold $N^* = 3.32 \text{ eV}/1 \times 10^{-5} \text{ eV/cation} = \sim 3 \times 10^5$ cations for pure Kr. To estimate how far above this trapping threshold our experimental conditions are, we combine empirical evidence [23] and charged particle trajectory simulations using the initial photocation distribution generated in our experiments (not shown). The result yields the approximate relation $N_e/N^* = 1/(1-T)^2$ where T is the electron trapping fraction. Thus, $N_e/N^* \sim 5$ for $T = 56\%$ in an atomic beam of pure Kr ionized by $80 \text{ }\mu\text{J}$ of 214.7 nm laser light. Estimating the total number of photoelectrons from the image intensity divided by the average intensity of a single electron hit, the experimental estimate of N^* is 1.5×10^6 for pure Kr. We consider this reasonable agreement, given the unknown impact of gradients in the ion and electron density and expected nonlinearities in the MCP response. The dynamics of electron trapping and escape could be complicated by the asymmetry in the initial spatial distributions of photoelectrons and photocations. Future experiments could reduce gain and signal saturation by using a position sensitive detector with less gain (e.g., a single-plate MCP) or by increasing the size of the VMI image by increasing the flight length of the mass spectrometer.

Dynamical information on the plasma electron distribution can be obtained by analyzing the *size* and *shape* of the velocity-mapped image. After the escaping electron contribution has decayed away, velocity-mapped images of the extracted plasma electrons are approximately isotropic with an intensity maximum at the image center (compare inset images collected at 20 ns , $0.5 \text{ }\mu\text{s}$, and $2 \text{ }\mu\text{s}$ in Fig. 3). This symmetry justifies a binning procedure to reduce the crushed 3D information in each image to a radial, 1-dimensional (1D) velocity distribution as shown in Fig. 4. For the Kr REMPI plasma prepared in this experiment, the 1D velocity distributions of the trapped electron distribution evolve in time from non-Gaussian to an approximately Gaussian line shape. From gas-kinetic theory, the Maxwell-Boltzmann velocity distribution (MBVD), $(m_e/2\pi k_B T)^{3/2} 4\pi v^2 e^{-mv^2/2k_B T}$, corresponds to identical 1D Gaussian velocity distributions along each of the three Cartesian dimensions, $(m_e/2\pi k_B T)^{1/2} e^{-mv_i^2/2k_B T}$, where $i \in x, y, z$. Although it is not possible for the expanding plasma to reach global thermodynamic equilibrium, we can estimate bounds on the timescale for establishing local *electron* thermodynamic equilibrium. The lower bound on this timescale is dictated by the reciprocal of the electron plasma frequency $2\pi/\omega_e = \sqrt{m_e \epsilon_0 / \rho_e e^2}$, which is $\sim 60 \text{ ps}$ in this experiment. Previous charged particle trajectory modeling of ultracold plasmas produced at the higher densities achieved in a Bose-Einstein condensate suggest that the average electron energy converges on a timescale very close to the reciprocal of the electron plasma frequency (8 ps) [12]. However, at the initial photoelectron energy and density of the pure Kr beam, estimating electron-electron equilibration

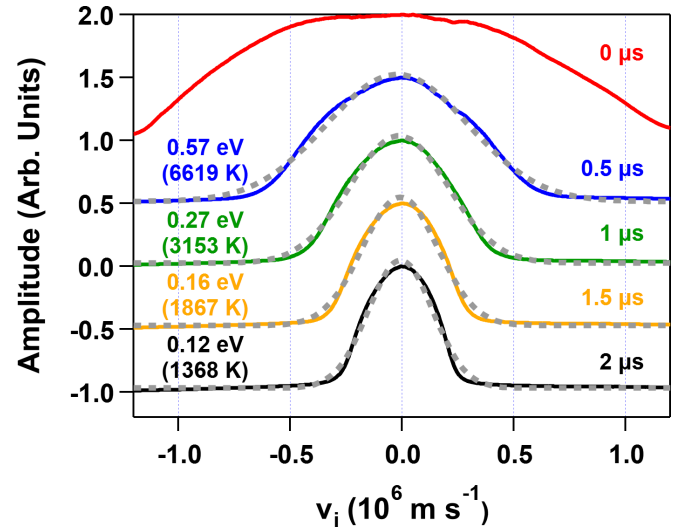


FIG. 4. One-dimensional data obtained by vertically binning velocity-mapped images. In the limit of an angularly isotropic electron energy distribution, these plots should correspond to one-dimensional electron velocity distributions averaged over all plasma electrons. Although the system is not in global thermodynamic equilibrium, traces at 0.5 , 1.0 , 1.5 , and $2.0 \text{ }\mu\text{s}$ are reasonably well described by a single Gaussian (dashed gray lines). The energy and temperature associated with each Gaussian fit is included for reference. The measurement resolution is $\sim 1400 \text{ m/s}$.

with a Fokker-Planck approach suggests that the electron equilibration time could be as large as $\sim 200 \text{ ns}$ [28]. Our data suggest that the spatially averaged electron velocity distribution is only well approximated by a single-temperature MBVD after approximately $0.5 \text{ }\mu\text{s}$. At earlier times, the spatial average is more complex and possibly more sensitive to shot-to-shot variations in laser power and distortion from the dense photocation distribution. To give an approximate feel for the evolving energy distribution within the plasma, Fig. 4 includes effective temperatures obtained from Gaussian fits. The electron temperatures and corresponding energies decay from 6619 K and 0.57 eV at $0.5 \text{ }\mu\text{s}$ to 1368 K and 0.12 eV at $2 \text{ }\mu\text{s}$. Although Fig. 4 tracks dramatic changes in the plasma velocity distribution at time intervals of $0.5 \text{ }\mu\text{s}$, it is important to note that our VMI apparatus can monitor changes with nanosecond resolution as evidenced by our ability to resolve differences in the escaping electron distribution (see Fig. 3). The monotonic contraction of the experimental 1D velocity distributions shown in Fig. 4 has a $0.24 \text{ }\mu\text{s}$ timescale ($1/e$) and can be associated with cooling induced by plasma expansion (the experimental timescale is roughly consistent with analytical predictions for a spherical Gaussian plasma when the size is set to the long axis of the ellipsoidal plasma [24]). Electron evaporation, identified as the slow ($\tau \sim 1 \text{ }\mu\text{s}$) decay timescale in the extracted electron signal in Fig. 3, should be controlled by the steady decrease of the cation Coulomb potential as the Kr plasma expands in vacuum.

IV. CONCLUSION

We have demonstrated the utility of velocity-mapped imaging with an ultrafast, high-voltage extraction pulse for monitoring the dynamics of a plasma induced by 2+1 REMPI

on timescales ranging from nanoseconds to microseconds. Nanosecond resolution allows us to monitor and quantify photoelectron escape, electron trapping induced by the resulting charge imbalance, and cooling of the electron energy distribution associated with electron loss as the cationic plasma expands into vacuum. Ultrafast extraction and velocity-mapped imaging of laser-induced plasmas represent a needed synthesis of ideas from the atomic, molecular, and plasma physics communities. Ion optics can be designed to ensure all electrons in a specific volume with velocities directed into all 4π sr are extracted and imaged on a position sensitive detector. Microchannel plate electron multipliers offer excellent sensitivity to the extracted electrons (between 50% and 85%), are sensitive enough to detect single electrons, and saturation can be avoided by selecting a stack with lower gain or by spreading the velocity-mapped plasma image over a larger area. With further development, this technique has the potential to interrogate currently inaccessible electron equilibration dynamics in ultracold plasmas [24]. Given that the electron energy distribution is a crucial plasma parameter controlling chemistry induced by the plasma, internal plasma

speciation via electron-impact excitation and ionization, and thermodynamic properties of the plasma such as conductivity and viscosity [10], ultrafast extraction, and velocity-mapped imaging measurements should complement existing methods and find general use in the optimization of plasma technology.

ACKNOWLEDGMENTS

This material is based upon work supported by the Division of Chemical Sciences, Geosciences and Biosciences, Office of Basic Energy Sciences (BES), U.S. Department of Energy (USDOE). Sandia National Laboratories is a multimission laboratory managed and operated by National Technology and Engineering Solutions of Sandia, LLC, a wholly owned subsidiary of Honeywell International, Inc., for the USDOE's National Nuclear Security Administration under Contract No. DE-NA-0003525. This paper describes objective technical results and analysis. Any subjective views or opinions that might be expressed in the paper do not necessarily represent the views of the USDOE or the U.S. Government.

-
- [1] H. Conrads and M. Schmidt, *Plasma Sources Sci. Technol.* **9**, 441 (2000).
- [2] J. P. Rayner, A. P. Whichello, and A. D. Cheetham, *IEEE Trans. Plasma Sci.* **32**, 269 (2004).
- [3] Y. Wang, M. Craven, X. Yu, J. Ding, P. Bryant, J. Huang, and X. Tu, *ACS Catal.* **9**, 10780 (2019).
- [4] P. J. Bruggeman *et al.*, *Plasma Sources Sci. Technol.* **25**, 053002 (2016).
- [5] A. Bogaerts *et al.*, *J. Phys. D: Appl. Phys.* **53**, 443001 (2020).
- [6] V. Godyak and V. Demidov, *J. Phys. D: Appl. Phys.* **44**, 233001 (2011).
- [7] L. Heroux, *Proc. Phys. Soc.* **83**, 121 (1964).
- [8] J. Torres, J. M. Palomares, A. Sola, J. J. A. M. van der Mullen, and A. Gamero, *J. Phys. D: Appl. Phys.* **40**, 5929 (2007).
- [9] R. F. Boivin, J. L. Kline, and E. E. Scime, *Phys. Plasmas* **8**, 5303 (2001).
- [10] K. Warner and G. M. Hieftje, *Spectrochim. Acta B* **57**, 201 (2002).
- [11] J. L. Roberts, C. D. Fertig, M. J. Lim, and S. L. Rolston, *Phys. Rev. Lett.* **92**, 253003 (2004).
- [12] T. Kroker, M. Großmann, K. Sengstock, M. Drescher, P. Wessels-Staermann, and J. Simonet, *Nat. Commun.* **12**, 596 (2021).
- [13] X. L. Zhang, R. S. Fletcher, and S. L. Rolston, in *Non-neutral Plasma Physics VII: 9th International Workshop on Non-neutral Plasmas*, edited by J. R. Danielson and T. S. Pedersen, AIP Conf. Proc. No. 1114 (AIP, Melville, NY, 2009), p. 11.
- [14] R. Haenel, M. Schulz-Weiling, J. Sous, H. Sadeghi, M. Aghigh, L. Melo, J. S. Keller, and E. R. Grant, *Phys. Rev. A* **96**, 023613 (2017).
- [15] A. T. J. B. Eppink and D. H. Parker, *Rev. Sci. Instrum.* **68**, 3477 (1997).
- [16] D. W. Chandler and P. L. Houston, *J. Chem. Phys.* **87**, 1445 (1987).
- [17] D. M. Neumark, *J. Phys. Chem. A* **112**, 13287 (2008).
- [18] D. Nandi, V. S. Prabhudesai, E. Krishnakumar, and A. Chatterjee, *Rev. Sci. Instrum.* **76**, 053107 (2005).
- [19] D. W. Chandler, J. W. Thoman, M. H. M. Janssen, and D. H. Parker, *Chem. Phys. Lett.* **156**, 151 (1989).
- [20] M. Ahmed, D. S. Peterka, and A. G. Suits, *Chem. Phys. Lett.* **301**, 372 (1999).
- [21] T. R. Sharples, J. G. Leng, T. F. M. Luxford, K. G. McKendrick, P. G. Jambrina, F. J. Aoiz, D. W. Chandler, and M. L. Costen, *Nat. Chem.* **10**, 1148 (2018).
- [22] D. W. Chandler, P. L. Houston, and D. H. Parker, *J. Chem. Phys.* **147**, 013601 (2017).
- [23] T. C. Killian, S. Kulin, S. D. Bergeson, L. A. Orozco, C. Orzel, and S. L. Rolston, *Phys. Rev. Lett.* **83**, 4776 (1999).
- [24] T. C. Killian, T. Pattard, T. Pohl, and J. M. Rost, *Phys. Rep.* **449**, 77 (2007).
- [25] S. Kulin, T. C. Killian, S. D. Bergeson, and S. L. Rolston, *Phys. Rev. Lett.* **85**, 318 (2000).
- [26] M. Schulz-Weiling, H. Sadeghi, J. Hung, and E. Grant, *J. Phys. B: At. Mol. Opt. Phys.* **49**, 193001 (2016).
- [27] M. A. Dakka, G. Tsiminis, R. D. Glover, C. Perrella, J. Moffatt, N. A. Spooner, R. T. Sang, P. S. Light, and A. N. Luiten, *Phys. Rev. Lett.* **121**, 093201 (2018).
- [28] K. S. Thorne and R. D. Blandford, *Modern Classical Physics: Optics, Fluids, Plasmas, Elasticity, Relativity, and Statistical Physics* (Princeton University Press, Princeton, NJ, 2017).